

## Supporting Information

# Anisotropic Signal Processing with Trigonal Selenium Nanosheet Synaptic Transistors

*Jing-Kai Qin<sup>1,3</sup>, Feichi Zhou<sup>1</sup>, Jingli Wang<sup>1,2</sup>, Jiewei Chen<sup>1</sup>, Cong Wang<sup>1</sup>, Xuyun Guo<sup>1</sup>, Shouxin Zhao<sup>3</sup>, Yi Pei<sup>3</sup>, Liang Zhen<sup>3</sup>, Peide D. Ye<sup>4</sup>, Shu Ping Lau<sup>1,2</sup>, Ye Zhu<sup>1</sup>, Cheng-Yan Xu<sup>3</sup>, and Yang Chai<sup>1,2\*</sup>*

<sup>1</sup>Department of Applied Physics, The Hong Kong Polytechnic University, Hung Hom, Kowloon, Hong Kong 999077, People's Republic of China

<sup>2</sup>The Hong Kong Polytechnic University Shenzhen Research Institute, Shenzhen 518055, People's Republic of China

<sup>3</sup>School of Materials Science and Engineering, Harbin Institute of Technology (Shen Zhen), Shen Zhen 518055, People's Republic of China

<sup>4</sup>School of Electrical and Computer Engineering, Purdue University, West Lafayette, Indiana 47907, United States

\*Address correspondence to: ychai@polyu.edu.hk

The *t*-Se is intrinsic 1D van der Waals (vdW) materials, where Se atoms are covalently bonded along *c*-axis direction in the form of 1D atomic chains while stacked radially along the perpendicular directions *via* weak vdW interaction. Therefore, 2D *t*-Se nanosheets tend to crystallize in an irregular quadrangular shape with the straight edge along the *c*-axis direction, and we can easily judge the crystal orientation from optical microscopy image (**Fig. S1a**). Angle-resolved Raman spectroscopy was also conducted to investigate the in-plane anisotropy of *t*-Se nanosheet. Here,  $\theta$  is defined as the angle between laser polarization direction and straight edge of the nanosheet. During measurement, it can be tuned by rotating the sample in a step of 15°. **Fig. S1c** shows the typical Raman spectrum of 28 nm thick nanosheet with the angle  $\theta$  of 30°, and obvious intensity change with dependent of  $\theta$  can be demonstrated. We can extract the peak intensity of modes and plot it into polar figures (**Fig. S1d**). The E<sub>2</sub> has the maximum value at about

45°, while  $A_1$  mode reaches the maximum at an angle of  $\sim 90^\circ$ , coinciding with the direction vertical to the straight edge of Se nanosheet. HRTEM was finally performed to confirm the crystal orientation as shown in **Fig. S1b**, where distinct 1D Se atomic chains can be observed along the straight edge direction. In this way, we could demonstrate the in-plane anisotropy and identify the crystal orientation of *t*-Se nanosheet.

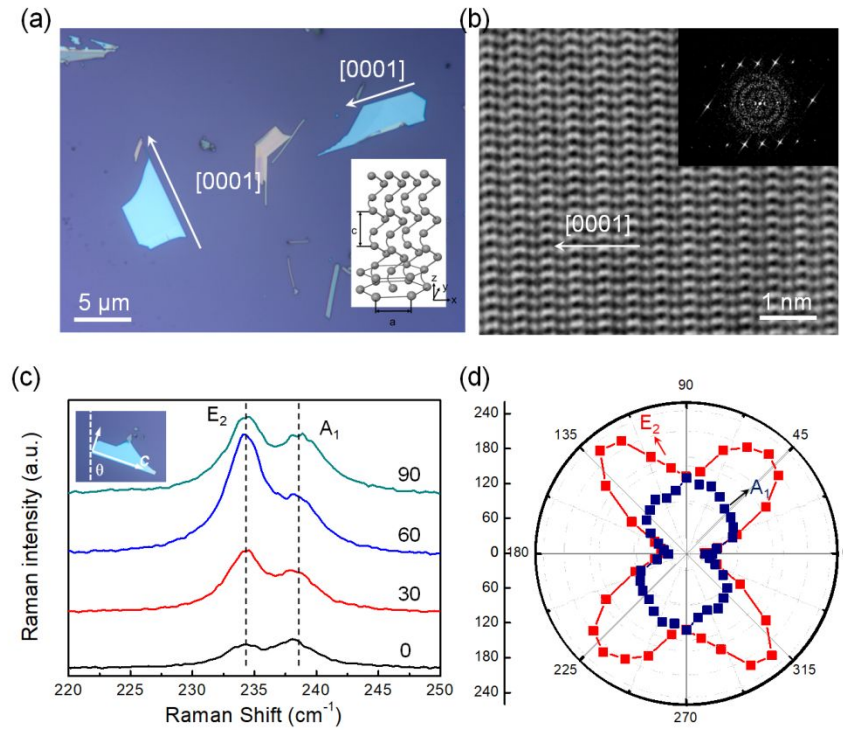


**Figure S1.** (a) Optical microscopy image of samples after transferred onto the  $\text{SiO}_2/\text{Si}$  substrate. (b) HRTEM image and corresponding SAED pattern of *t*-Se nanosheets. (c) Raman spectra evolution with angles between crystal orientation and incident laser polarization. (d) Polar figures of Raman intensity of  $E_2$  and  $A_1$  modes.

The testing environment has negligible influence on the performance of devices. As the typical transfer curves shown in **Fig. S2**, the curve of as-fabricated device obtained in air is very close to that achieved in vacuum environment. The device also exhibits an excellent air-stability. After 3-day-exposure in air, insignificant degradation of electrical properties was observed. The great air-stability can be attributed to the dense solid-state electrolyte film covered on the device,

which can well shield the channel materials from external environment.

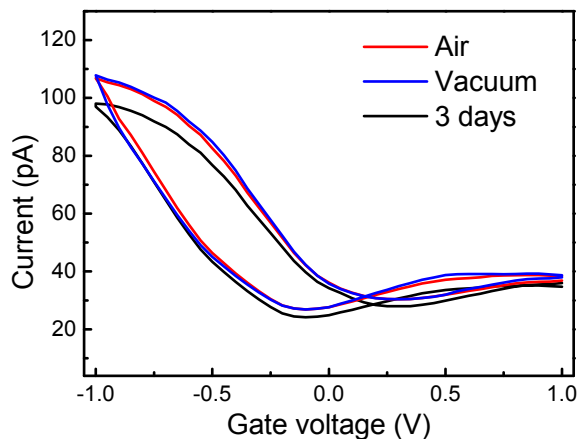


**Figure S2.** Transfer characteristic of a typical *t*-Se EGT device measured as fabricated and after 3 days storage in air and vacuum condition.

Under positive voltage pulse,  $\text{Li}^+$  ion would intercalate into the lattice of *t*-Se, and result into the formation a  $\text{Li}_x\text{Se}$  phase. Such new phase is expected to have lower conductivity and lead to the reduction of channel electrical conductance, which was demonstrated by theoretical calculations (**Figure S3**). The band gap of  $\text{Li}_2\text{Se}$  is calculated to be 2.97 eV, which is much larger than Se (1.5 eV), suggesting a worse electrical conductivity of  $\text{Li}_2\text{Se}$ .

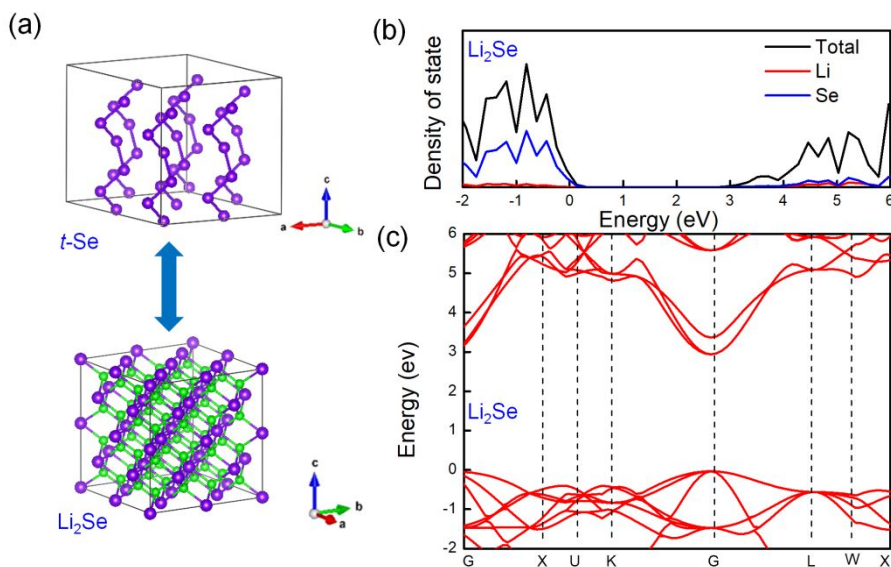


**Figure S3.** (a) The schematic illustration of reversible phase transition from Se to  $\text{Li}_2\text{Se}$ . (b-c) Density of

states and band structure of  $\text{Li}_2\text{Se}$ . The band gap of  $\text{Li}_2\text{Se}$  is calculated to be 2.97 eV, which is much larger than Se (1.5 eV), suggesting a worse electrical conductivity of  $\text{Li}_2\text{Se}$ .

**Figure S4** compares the Raman spectra of *t*-Se nanosheet obtained before and after  $\text{Li}^+$  intercalation. After the  $\text{Li}^+$  intercalation, both the  $\text{E}_2$  and  $\text{A}_1$  modes of *t*-Se move to the higher direction, which is attributed to the phase change as well as the charge transfer between  $\text{Li}^+$  ion and *t*-Se.

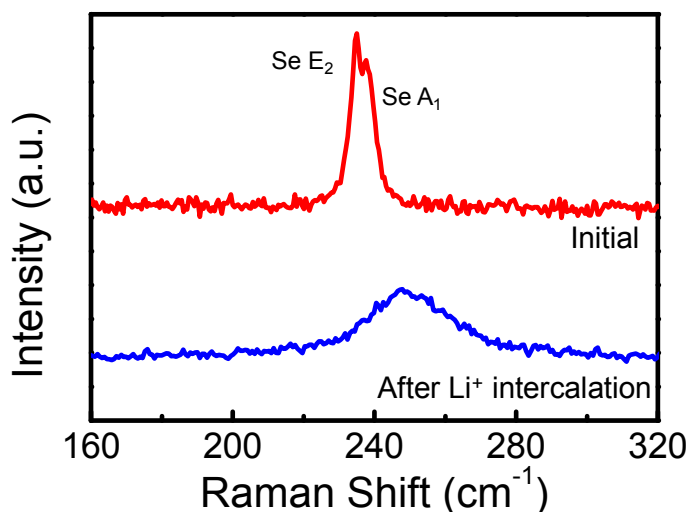


**Figure S4.** Raman spectra of the *t*-Se NS before and after  $\text{Li}^+$  intercalation. After the  $\text{Li}^+$  intercalation, both the  $\text{E}_2$  and  $\text{A}_1$  modes move to the higher direction, which is attributed to the phase change of *t*-Se.

The device covered with PEO/ $\text{LiClO}_4$  solid-state electrolyte was immersed into methanol at temperature of 50 °C for 30 min we after the electrical measurement, and the electrolyte can be completely removed. We conducted AFM characterization, electrical measurement and HRTEM characterization to demonstrate the change of *t*-Se nanosheet as a result of  $\text{Li}^+$  intercalation. As shown in **Fig. S5a** and **S5b**, the integrity of *t*-Se nanosheet was well maintained after removing the electrolyte. The thickness increases slightly from original 22 nm to 28 nm, and it is in agreement with the cross-sectional TEM characterization (**Fig. S5d** and **S5e**), where distinct thickness increase of *t*-Se can be observed after the  $\text{Li}^+$  intercalation. The transfer curve of device shows a significant drop of on-state current, as shown in **Fig. S5c**. The change of thickness and

electrical performance can be understood as a result of the phase change from Se to  $\text{Li}_x\text{Se}$  occurred during  $\text{Li}^+$  intercalation.

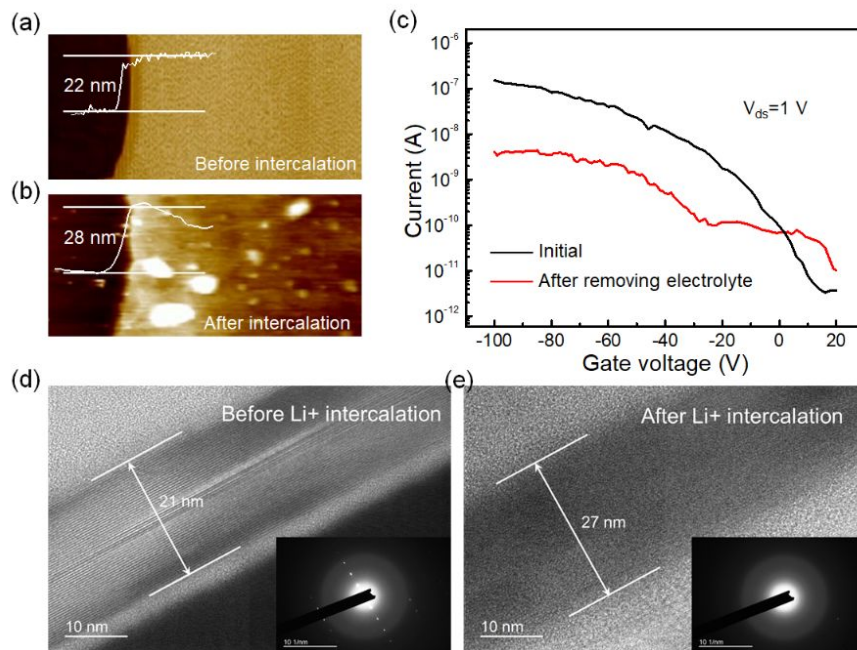


**Figure S5.** (a,b) AFM characterization of Se channel before and after the  $\text{Li}^+$  intercalation. (c) Transfer curves of a  $t$ -Se back-gate transistor. (d-e) Cross-section HRTEM image and corresponding selected area electron diffraction (SAED) pattern of  $t$ -Se before and after  $\text{Li}^+$  intercalation.

To demonstrate the reproducibility, we fabricated more two-terminal EGT devices on the basis of  $t$ -Se nanosheets with the different thickness, and conducted both DC and pulse measurements, as shown in **Figure S6**. The hysteresis in the transfer curve caused by the  $\text{Li}^+$  intercalation/extraction can be clearly observed and well reproduced, and all the device exhibits a clear long-term change of channel conductance after applying a single gate pulse (2 V, 1000 ms). We summarized the long-term change of PSC ( $\Delta G/G_0$ ) of devices (**Figure S7**), and it tends to drop gradually with the increase of thickness of  $t$ -Se, which can be well explained by higher intercalation efficiency of Li ion in thinner samples.

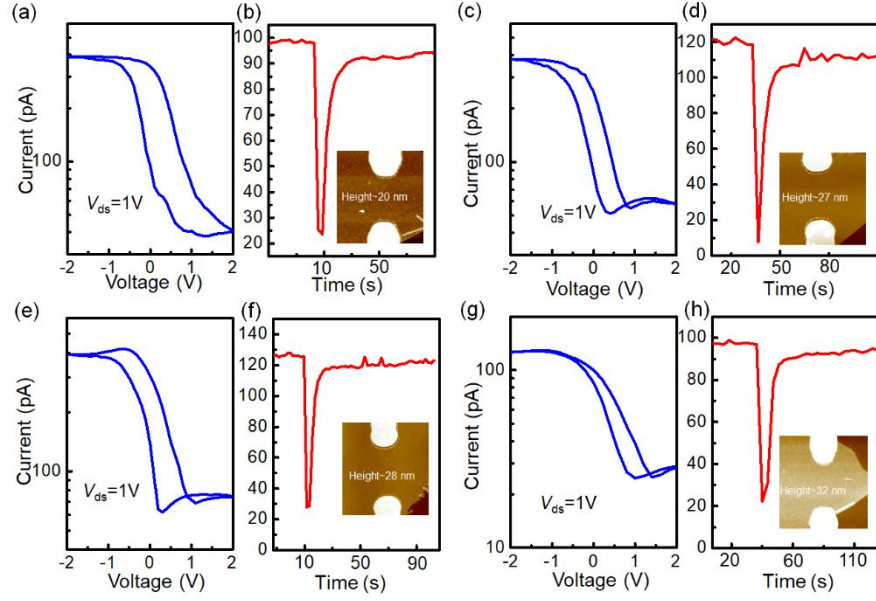


**Figure S6.** Transfer curve and time-dependent current change after applying voltage pulse (2 V, 1000 ms) of two-terminal EGT devices with different thickness. The inset image shows the corresponding AFM height profile of t-Se nanosheet.

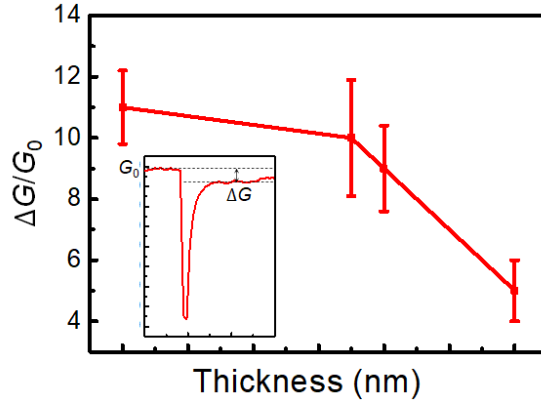


**Figure S7.** Dependence of long-term weight changes on the thickness of t-Se nanosheet.

The power consumption per operation can be calculated by  $P = V_{ds} \times \Delta I \times t_{on}$ , where  $V_{ds}$ ,  $\Delta I$  and  $t_{on}$  represent source-drain voltage, EPSC and the pulse width, respectively. **Figure S8** plots the change ratio of energy consumption as a function of pulse width. The smallest energy consumption was calculated to be only 0.1 pJ for a single pulse (2.0 V) event. **Table S1** compares the energy consumption of t-Se EGT devices between other devices with the similar configuration.

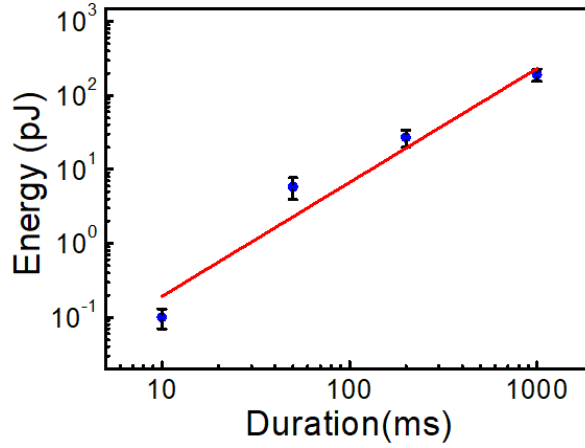


**Figure S8.** The corresponding energy consumption with the dependence of pulse width for “read” operation.

**Table S1.** Synaptic characteristics of three-terminal electrolyte-gating transistor

Channel	Electrolyte	Ion	Linearity	Conductance	Energy	Ref
Carbon nanotube	PEG	H <sup>+</sup>	-	45 nS	7.5 pJ	1
a-MoO <sub>3</sub>	Ionic liquid	H <sup>+</sup>	0.2	95nS	0.2 pJ	2
PEDOT:PPS/PEI	KCl	H <sup>+</sup>	0.1	850 uS	10 pJ	3
a-MoO <sub>3</sub>	LiClO <sub>4</sub> /PEO	Li <sup>+</sup>	0.31	75nS	0.16 pJ	4
WSe <sub>2</sub>	LiClO <sub>4</sub> /PEO	Li <sup>+</sup>	0.15	2 pS	0.03 pJ	5
<i>t</i> -Se	LiClO <sub>4</sub> /PEO	Li <sup>+</sup>	0.11	4 pS	0.1 pJ	This work

Consecutive positive voltage pulse would result into the long-term plasticity of *t*-Se EGT devices, while the subsequent negative voltage pulse can help recover the channel conductance as shown in **Figure S9**. It can be well explained by the extraction of Li<sup>+</sup> and reversible phase change from Li<sub>x</sub>Se to *t*-Se.

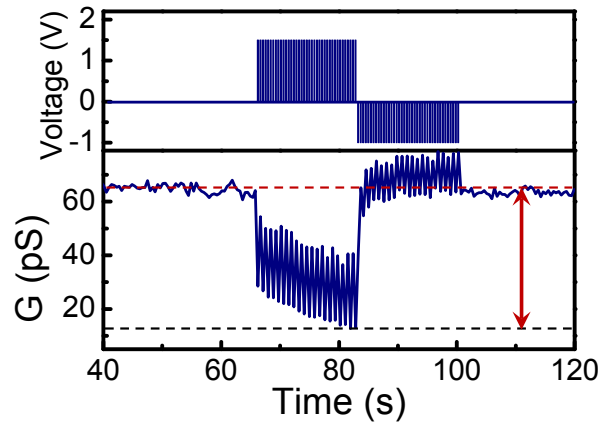


**Figure S9.** Synaptic depression and potentiation process realized by applying successive positive ( $V_g = 1.5$

$V$ ,  $t_{on} = 200$  ms,  $\Delta t = 1$  s) and negative voltage spikes ( $V_g = -1.0$  V,  $t_{on} = 200$  ms,  $\Delta t = 1$  s). Consecutive positive voltage pulses result in the long-term plasticity of  $t$ -Se EGT devices, while the subsequent negative voltage pulse can help recover the channel conductance due to the extraction of  $Li^+$  and reversible phase change from  $Li_xSe$  to  $t$ -Se.

The successive negative voltage spikes cannot result into the long-term change of conductance in devices, as shown in **Figure S10**. Channel conductance will recover back after 10 consecutive voltage spikes, since  $ClO_4^-$  ions with relatively larger size are very difficult to intercalate into  $t$ -Se crystal lattice.

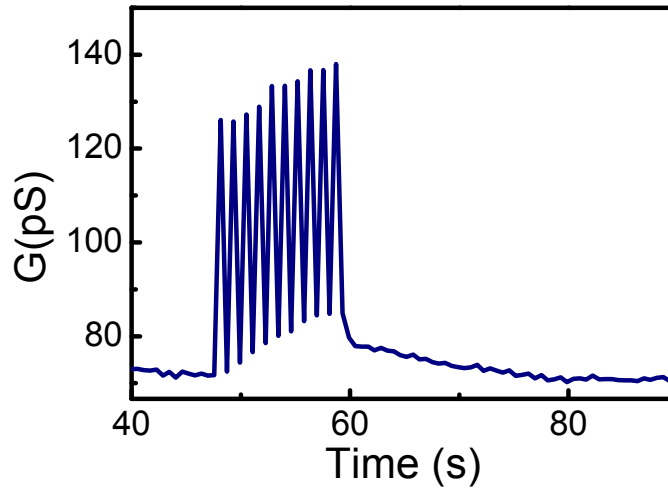


**Figure S10.** Long-term potentiation process of synapse as applied with a successive gate voltage ( $V_g = -1.5$  V,  $t_{on} = 200$  ms,  $\Delta t = 1$  s). Only the successive negative voltage spikes cannot result into the long-term change of conductance in devices, since  $ClO_4^-$  ions with relatively larger size are very difficult to intercalate into  $t$ -Se crystal lattice.

Four-terminal back-gate field effect transistor was fabricated to investigate the anisotropy of electrical transport properties in 2D  $t$ -Se (**Figure S11a-b**). Carrier mobility can be extracted from the transfer curves, and it is calculated to be  $0.64 \text{ cm}^2/(\text{Vs})$  along  $c$ -axis. However, it will decrease to only  $0.11 \text{ cm}^2/(\text{Vs})$  along the perpendicular direction (**Figure S11c**). The corresponding output curve indicates an ideal Ohmic contact at Pt/ $t$ -Se interface (**Figure S11d**). The conductance along



Se atomic chain is estimated to be an order of magnitude larger than that of the orthogonal direction, and the maximum anisotropic ratio up to 8.6 can be obtained at  $V_g$  of  $-100$  V.

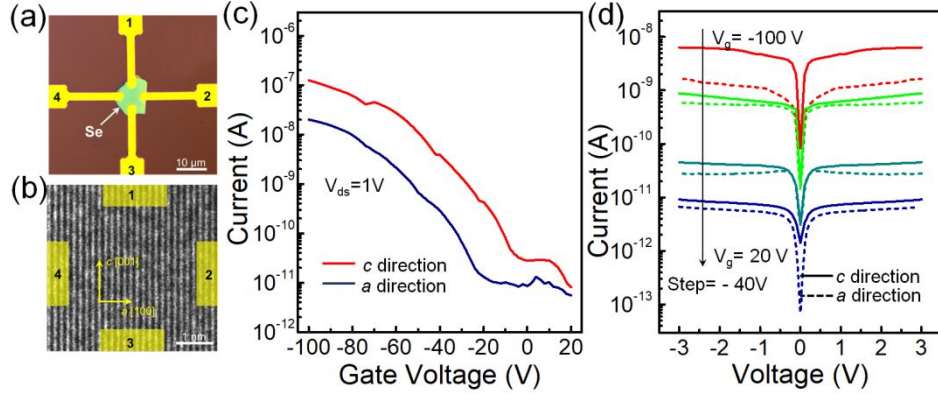


**Figure S11.** Four-terminal back-gate field effect transistor was fabricated to investigate the anisotropy of electrical transport properties in *t*-Se nanosheet. **(a)** The optical image and **(b)** HRTEM image of the *t*-Se field-effect transistor with a pair of opposite electrodes. The electrodes 1 and 3 are patterned along *c* [001] direction, while electrodes 2 and 4 are across the direction. **(c)** The transfer characteristic of devices along *c* and *a*-axis direction with drain-source bias of 1 V. **(d)** The direction-dependent I-V characteristics with applied back gate voltage  $V_g$  ranging from -100 to 20 V.

As shown in **Figure S12**, the capping of BN layers on electrodes could significantly reduce the gate leakage current to pA level, which helps ensure the gate control over the channel conductance.

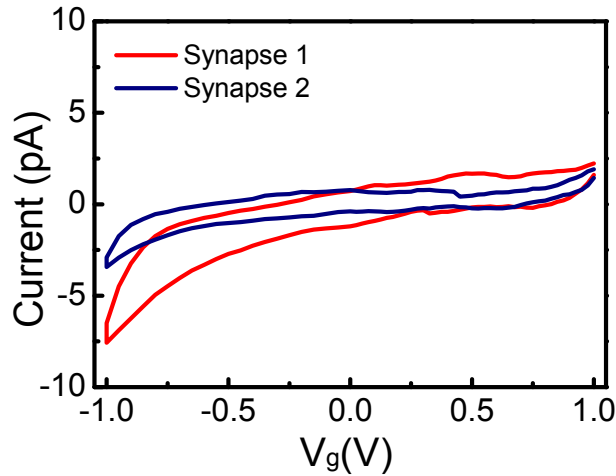


**Figure S12.** The leakage current on dependence of gate voltage in the multi-terminal *t*-Se EGT devices. The capping of BN layers on electrodes could significantly reduce the gate leakage current to pA level, which helps ensure the gate control over the channel conductance.

The EGT devices along the different crystal orientation exhibit anisotropic response towards the same input stimulus. **Figure S13** compare the response of channel conductance in multi-terminal device to stimulus train with different frequency (2, 5 and 10 Hz). As a high-passing filter, the amplitude gains of synapse 2 increases sharply at high frequency with the highest value of 280% at 10 Hz, while the synapse 1 exhibits very weak response to the frequency and the amplitude gain is only 150%.

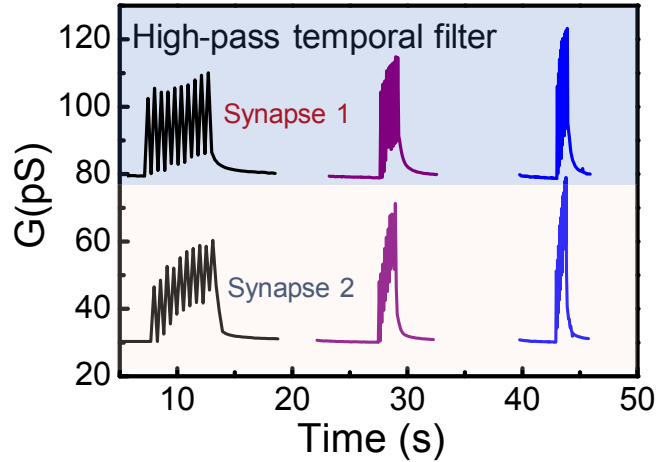


**Figure S13.** The responses of conductance triggered by trains of presynaptic spikes ( $-1$  V, 100 ms) with frequencies of 2, 5 and 10 Hz. The EGT devices along the different crystal orientation exhibit anisotropic response towards the same input stimulus, showing its great potential as new-function high-pass temporal filter

We fabricated more four-terminal devices on basis of *t*-Se nanosheets with thickness ranging from 22 to 40 nm, as the typical transfer curves shown in **Figure S14**. It is clear that *c*-axis device shows much higher channel current compared with *a*-axis device, while the on-off ratio of *c*-axis device is much lower than that along the perpendicular direction.

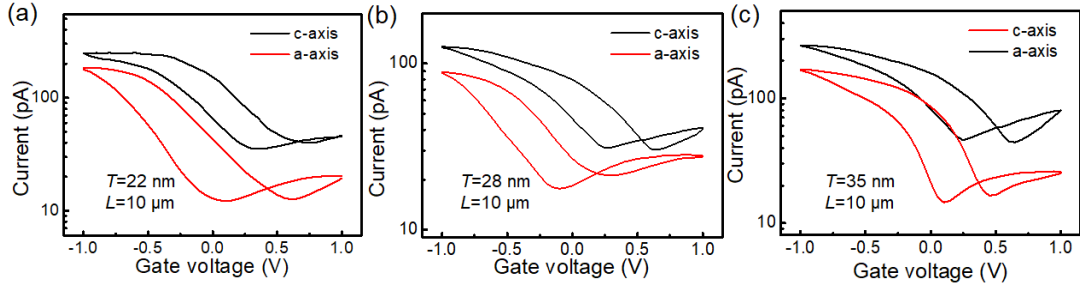


**Figure S14.** The typical transfer curves of the *t*-Se EGT devices with different thickness (a) 22 nm; (b) 28 nm; (c) 35 nm. *c*-axis device shows much higher channel current compared with *a*-axis device, while the on-off ratio of *c*-axis device is much lower than that along the perpendicular direction.

Consecutive voltage pulse ( $V=\pm 1V$ ,  $t_{on}=100$  ms) was also applied through side gate with frequency ranging from 1 to 10 Hz, and the frequency-dependent amplitude gains/reductions are extracted on basis of such four-terminal devices. **Figure S15** plot the amplitude gains as well as amplitude reductions of *t*-Se EGT devices with thickness of 22, 28 and 35 nm, respectively. All the devices exhibit distinct anisotropy in their filtering ability, which suggest a great reproducibility of *t*-Se EGT devices.

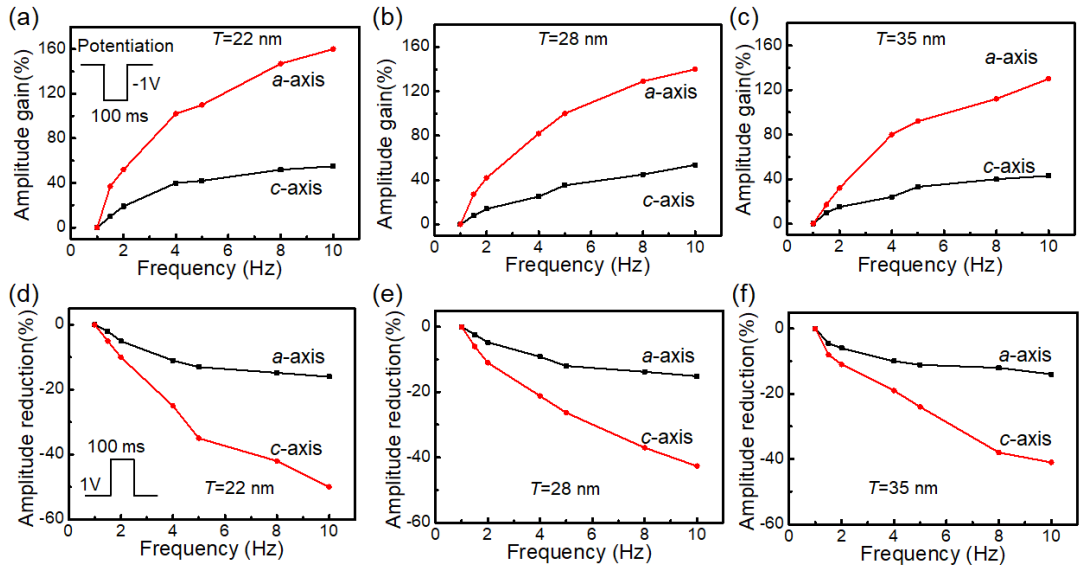


**Figure S15.** (a-c) Frequency-dependent amplitude gain ( $A_{10}/A_1$ ) and (d-e) amplitude reduction of *t*-Se devices with different thickness frequency. All the devices exhibit distinct anisotropy in their filtering

-

behavior, which suggests a good reproducibility of *t*-Se EGT devices.

## Reference

1. Kim, K.; Chen, C.-L.; Truong, Q.; Shen, A.M.; Chen, Y. A Carbon Nanotube Synapse with Dynamic Logic and Learning. *Adv. Mater.* **2013**, *25*, 1693-1698.
2. Yang, C. S.; Shang, D. S.; Liu, N.; Shi, G.; Shen, X.; Yu, R. C.; Li, Y. Q.; Sun, Y. A Synaptic Transistor Based on Quasi-2D Molybdenum Oxide. *Adv. Mater.* **2017**, *29*, 1700906.
3. van de Burgt, Y.; Lubberman, E.; Fuller, E. J.; Keene, S. T.; Faria, G. C.; Agarwal, S.; Marinella, M. J.; Talin, A. A.; Salleo, A. A Non-Volatile Organic Electrochemical Device as a Low-Voltage Artificial Synapse for Neuromorphic Computing. *Nat. Mater.* **2017**, *16*, 414-418.
4. Yang, C. S.; Shang, D. S.; Liu, N.; Fuller, E. J.; Agrawal, S.; Talin, A. A.; Li, Y. Q.; Shen, B. G.; Sun, Y. All-Solid-State Synaptic Transistor with Ultralow Conductance for Neuromorphic Computing. *Adv. Funct. Mater.* **2018**, *28*, 1804170.
5. Zhu, J.; Yang, Y.; Jia, R.; Liang, Z.; Zhu, W.; Rehman, Z. U.; Bao, L.; Zhang, X.; Cai, Y.; Song, L. Ion Gated Synaptic Transistors Based on 2D van der Waals Crystals with Tunable Diffusive Dynamics. *Adv. Mater.* **2018**, *30*, 1800195.